Comprehensive Investigation of Factors Affecting Acid Fracture Propagation with Natural Fracture

Qingdong Zeng [1], Taixu Li [1], Long Bo [1], Xuelong Li [1,*] and Jun Yao [2]

1 College of Energy and Mining Engineering, Shandong University of Science and Technology, Qingdao 266590, China; upc.zengqd@163.com (Q.Z.); litaixv2025@163.com (T.L.); bl_sdkjdx@163.com (L.B.)

2 Research Center of Multiphase Flow in Porous Media, China University of Petroleum (East China), Qingdao 266580, China; upc_rcogfr@163.com

* Correspondence: lixlcumt@126.com

Abstract: Acid fracturing is a crucial stimulation technique to enhance hydrocarbon recovery in carbonate reservoirs. However, the interaction between acid fractures and natural fractures remains complex due to the combined effects of mechanical, chemical, and fluid flow processes. This study extends a previously developed hydro-mechano-reactive flow coupled model to analyze these interactions, focusing on the influence of acid dissolution. The model incorporates reservoir heterogeneity and simulates various scenarios, including different stress differences, approaching angles, injection rates, and acid concentrations. Numerical simulations reveal distinct propagation modes for acid and hydraulic fractures, highlighting the significant influence of acid dissolution on fracture behavior. Results show that hydraulic fractures are more likely to cross natural fractures, whereas acid fractures tend to be arrested due to wormhole formation. Increasing stress differences and approaching angles promote fracture crossing, while lower angles favor diversion into natural fractures. Higher injection rates facilitate fracture crossing by increasing pressure accumulation, but excessive acid concentrations hinder fracture initiation due to enhanced wormhole formation. The study demonstrates the importance of tailoring fracturing treatments to specific reservoir conditions, optimizing parameters to enhance fracture propagation and reservoir stimulation. These findings contribute to a deeper understanding of fracture mechanics in heterogeneous reservoirs and offer practical implications for improving the efficiency of hydraulic fracturing operations in unconventional reservoirs.

Keywords: acid fracturing; natural fracture; hydro-mechano-reactive flow model; phase field method; fracture propagation modes

1. Introduction

By injecting acidic solutions at high pressures, acid fracturing creates and propagates fractures while simultaneously dissolving the carbonate rock, resulting in increased permeability and improved connectivity within the reservoir. The presence of natural fractures adds complexity to this process, as the interaction between induced acid fractures and pre-existing natural fractures can significantly influence fracture propagation paths and, consequently, the efficiency of the stimulation, as shown in Figure 1. A comprehensive understanding of the factors affecting acid fracture propagation in naturally fractured reservoirs is essential for optimizing treatment designs and maximizing production.

Numerical studies have investigated the interactions between induced fractures and natural fractures in the context of hydraulic fracturing [1–4]. Yi et al. [5] proposed a coupled fluid flow and fracture phase field evolution model to simulate hydraulic fracture propagation in porous media with natural fractures. Their results demonstrated that smaller approaching angles, lower natural fracture strength, and smaller in situ stress differences make natural fractures more likely to initiate and propagate. Zhou et al. [6] advanced this understanding by developing a fully coupled hydro-mechanical model based

on the extended finite element method (XFEM) to handle different fracture interaction behaviors. Introducing a new weakly discontinuous junction enrichment function and adopting a tensile stress criterion for new fracture initiation, they investigated the effects of natural fracture properties, treatment parameters, matrix permeability, anisotropic stress, and intersection angle on fracture interaction. Xiong and Ma [7] developed a hydraulic fracture random propagation method using mesh node splitting and zero-thickness cohesive elements. Their study demonstrated that natural fractures could open and slip even without direct contact with hydraulic fractures, highlighting the influence of stress shadow effects and the importance of formation properties and injection rates on fracture complexity. Sun et al. [8] proposed a quantitative model to predict hydraulic fracture propagation across cemented natural fractures based on numerical simulation and developed a probability function to predict crossing behavior using logistic regression.
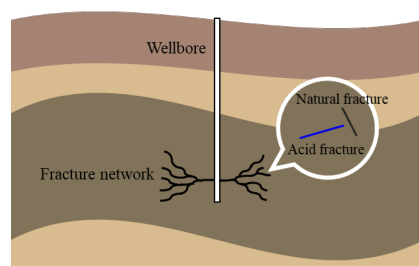
Figure 1. Schematic diagram of acid fracturing in naturally fractured reservoirs.

Experimental investigations have provided valuable insights into fracture propagation behavior in naturally fractured reservoirs [9–11]. Zhou et al. [12] conducted experimental studies using a tri-axial fracturing system, revealing complex interactions under various stress conditions and rock properties. Zhang et al. [13] performed experiments on hydraulic fracture propagation in tight sandstone formations with closed cemented natural fractures. By creating artificial tight sandstone specimens with controlled properties and embedded natural fractures, they showed that factors such as approach angle, in situ stress state, and natural fracture properties significantly influence the interaction between hydraulic and natural fractures. Qiu et al. [14] conducted laboratory tests to investigate the interaction between hydraulic fractures and natural fractures in deep unconventional reservoirs under high stress conditions and identified various interaction modes between hydraulic and natural fractures.

The topology and characteristics of natural fractures play a significant role in fracture network development. Wang et al. [15] investigated the role of natural fractures with different topology structures on hydraulic fracture propagation in continental shale reservoirs. Utilizing data from the Yanchang Formation, they classified natural fractures into three types based on node structures. Their study found that natural fractures with Type II nodes had the most substantial effect on inducing hydraulic fracture propagation and creating complex fracture networks. Injection parameters and fluid properties also critically impact fracture propagation. Li et al. [16] conducted a sensitivity analysis using a discrete fracture network (DFN) model based on outcrop data from the Ordos Basin, China. Their findings indicated that increasing natural fracture aperture decreased fracture complexity, while higher friction coefficients improved hydraulic fracturing efficiency. Higher injection rates led to more complex fracture networks, whereas higher fluid viscosity reduced fracturing efficiency. Tong et al. [17] proposed a new criterion for predicting the interaction between hydraulic fractures and natural fractures at non-orthogonal angles. Considering fluid flow, stress shadow effects, and poroelastic responses, they revealed that hydraulic fractures are more likely to cross natural fractures under conditions of short fracture half-length, high friction coefficient, high fluid viscosity, and high fracture toughness.

While significant progress has been made in understanding hydraulic fracture propagation, there is a relative paucity of studies specifically addressing acid fracture propagation in the presence of natural fractures. Acid fracturing introduces additional complexities

due to chemical reactions between the acid and the rock, which can alter fracture surfaces, change rock mechanical properties, and influence fracture propagation paths [18–20]. Dai et al. [21] conducted true triaxial acid fracturing experiments to study steering acid fracturing in carbonate reservoir and found that the complexity of fractures is influenced by natural fracture and the fluid viscosity. Chen et al. [22] addressed some of these complexities by simulating acid transport and dissolution in fracture networks using a 3D unified pipe-network method, allowing for the modeling of complex fracture geometries and their evolution due to acid dissolution. Zhu et al. [23] presented a discretized virtual internal bond approach for acid fracturing in complex fractured-vuggy carbonate reservoirs. By considering full hydro-mechanical-chemical coupling effects in large fractures and partial coupling in small fractures, their method could simulate large fracture propagation, interactions with natural fractures and cavities, and the activation of inactive natural fractures. Recently, we developed a hydro-mechano-reactive flow coupled model to simulate acid fracturing in heterogeneous reservoirs [24]. Despite these advancements, a comprehensive investigation integrating the various factors affecting acid fracture propagation with natural fractures remains lacking. Therefore, this study aims to fill this gap by conducting a comprehensive investigation into the factors affecting acid fracture propagation in the presence of natural fractures by extending the previously developed hydro-mechano-reactive flow coupled model.

This paper is structured as follows: Section 2 outlines the primary governing equation of the model, while Section 3 presents the numerical solution. Section 4 validates the model and provides an in-depth analysis of acid fracture propagation in conjunction with natural fractures. Finally, Section 5 offers some conclusions.

2. Governing Equations

Consider the scenario of an acid fracture approaching a natural fracture at an angle β, as illustrated in Figure 2. Acid fracture propagation encompasses acid transport, fluid flow, rock deformation, and fracture propagation. We present a hydro-mechano-reactive flow coupled model previously developed in [24]. This model is now extended to analyze the interaction between acid fractures and natural fractures. The study is based on the following assumptions: the fracturing process occurs under quasi-static and isothermal conditions; the reservoir is heterogeneous and saturated, accounting for variations in porosity, mineral inclusions, and elastic modulus; the fluid is compressible, and acid dissolution occurs instantaneously, following a first-order kinetic mechanism; principal stresses are considered. Limitations of the model include the following: it is a two-dimensional representation; the size of the research domain is constrained due to the small mesh scale required for accurate acid dissolution modeling. The main governing equations are provided for model completeness as follows.
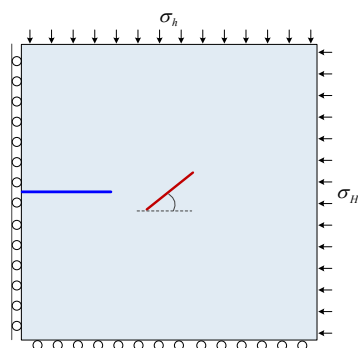
Figure 2. Schematic of interaction between acid fracture and natural fracture.

2.1. Reservoir Heterogeneity Characterization

Reservoir rock, at the microscopic level, comprises a solid matrix, pores, and mineral inclusions. Due to the random distribution of pores and minerals, the rock exhibits inherent

heterogeneity, affecting its macroscopic mechanical properties. Two scales are considered: the micro-scale, where pores disperse in the solid matrix forming a porous matrix, and the meso-scale, where mineral inclusions are distributed. A two-step linear homogenization approach, based on the Mori–Tanaka scheme [25,26], estimates the macroscopic mechanical parameters. This approach accounts for the heterogeneity of Young's modulus and Poisson's ratio of the rock. The acid dissolution modeling necessarily considers the heterogeneity of porosity, which in turn influences the heterogeneity of the rock's mechanical parameters. Furthermore, acid dissolution degrades the rock's mechanical modulus, significantly affecting fracture propagation. Therefore, it is crucial to account for the initial heterogeneity of the rock's mechanical parameters.

The first homogenization step accounts for the micro-scale pore effect, estimating the effective elastic stiffness of the porous medium as follows [27]:

$$C^{mp} = C^m : (I - f_p A^p) \tag{1}$$

where C^m is the elastic stiffness tensor of the solid matrix. I denotes the four-order unit tensor. F_p is the pores to matrix volume ratio, and Ap is the strain concentration tensor relating uniform strain to local strain:

$$A^p = (I - P^p : C^m)^{-1} : \left[(1 - f_p)I + f_p(I - P^p : C^m)^{-1} \right]^{-1} \tag{2}$$

where P_p represents the porous matrix's Hill tensor, determined by integrating the Green function [25,27].

The second homogenization step considers mineral inclusions, simplifying them into an equivalent phase to estimate rock's macroscopic effective elastic stiffness:

$$C^{hom} = C^{mp} + f_i(C^i - C^{mp}) : A^i \tag{3}$$

where A_i links macroscopic strain to local strain in inclusions:

$$A^i = \left[I + P^i : (C^i - C^{mp}) \right]^{-1} : \left[(1 - f_i)I + f_i\left(I + P^i : (C^i - C^{mp}) \right)^{-1} \right]^{-1} \tag{4}$$

where P_i is the macroscopic medium's Hill tensor, calculated similarly to P_p with C^{mp}.

2.2. Fluid Flow and Acid Transport

As fractures initiate and propagate, the properties of the damaged reservoir area change including compressibility, permeability, and Biot's coefficient. These are updated using Lee et al.'s linear interpolation approach [5]. Considering porosity alterations due to mineral dissolution, the fluid flow continuity equation is as follows:

$$\frac{\partial \phi}{\partial t} + S_t \frac{\partial p}{\partial t} + \nabla \cdot \left(-\frac{k_t}{\mu} \nabla p \right) = Q_0 - \alpha_t \frac{\partial \varepsilon_{vol}}{\partial t} \tag{5}$$

where S_t, k_t, and α_t are the medium's equivalent compressibility, permeability, and Biot's coefficient, calculated via interpolation [28]. Φ symbolizes porosity, μ is the fluid viscosity, and Q_0 is the source term.

Acid transport involves convection, dispersion, and transfer. The transfer term, describing acid flow to the fluid–solid interface, is a first-order kinetic reaction [29]:

$$R\left(C_f\right) = k_c\left(C_f - C_s\right) = k_s C_s = \frac{k_c k_s}{k_c + k_s} C_f \tag{6}$$

where k_c is the transfer coefficient, and k_s is the surface reaction rate. C_f and C_s are acid concentrations in the fluid phase and at the fluid–solid interface.

Acid transport's continuity equation is as follows:

$$\frac{\partial\left(\phi C_f\right)}{\partial t} + \nabla \cdot \left(v C_f\right) = \nabla \cdot \left(\phi \boldsymbol{D}_\mathrm{e} \cdot \nabla C_f\right) - a_v R\left(C_f\right) \tag{7}$$

where v is the fluid velocity. $\boldsymbol{D}_e$ denotes the effective dispersion tensor. Av denotes the specific surface area.

The transfer term changes porosity:

$$\frac{\partial\phi}{\partial t} = \frac{R\left(C_f\right) a_v \alpha_d}{\rho_s} \tag{8}$$

where α_d is the dissolving coefficient, and ρ_s is the rock's density.

Based on the two-scale continuum model [29], the pore structural parameters and related transfer coefficient and dispersion tensor are analyzed at the pore scale. Semi-empirical relations estimate the pore radius, permeability, and surface area due to porosity change:

$$\frac{r_p}{r_0} = \sqrt{\frac{k_r \phi_0}{k_0 \phi}} \tag{9}$$

$$\frac{k_r}{k_0} = \frac{\phi}{\phi_0}\left(\frac{\phi(1-\phi_0)}{\phi_0(1-\phi)}\right)^{2\gamma} \tag{10}$$

$$\frac{a_v}{a_0} = \frac{\phi r_0}{\phi_0 r_p} \tag{11}$$

where r_0, k_0, and α_0 denote initial average pore radius, permeability and surface area when porosity equals ϕ_0. Γ is the pore broadening parameter.

The transfer coefficient kc is derived via the Sherwood number:

$$Sh = \frac{2k_c r_p}{D_m} = Sh_\infty + 0.7\mathrm{Re}_p^{1/2} Sc^{1/3} \tag{12}$$

where D_m is molecular diffusivity, and Sh_∞ is the asymptotic Sherwood number. Rep is the Reynold's number, and Sc is the Schmidt number ($Sc = v_k/D_m$), where v_k is the kinetic velocity.

The dispersion tensor is characterized by longitudinal and transverse dispersion coefficients [29]:

$$D_{eX} = (\alpha_{os} + \lambda_X Pe_p)D_m \tag{13}$$

$$D_{eT} = (\alpha_{os} + \lambda_T Pe_p)D_m \tag{14}$$

where X and T denote acid injection and perpendicular directions. α_{os}, λ_X, and λ_T are pore-structure constants. Pep is the Peclet number, defined as Pep = $|v|d_h/(\phi D_m)$, where d_h is the pore's diameter.

2.3. Rock Deformation and Fracture Propagation

Considering elastic strain energy, crack surface energy, and fluid pressure dissipation energy, the porous medium's total energy functional is as follows:

$$\Psi(\boldsymbol{u},\Gamma,p) = \int_\Omega \psi(\boldsymbol{\varepsilon})\mathrm{d}\Omega + \int_\Gamma G_\mathrm{c}\mathrm{d}\Gamma - \int_\Omega \alpha_t p \cdot (\nabla \cdot \boldsymbol{u})\mathrm{d}\Omega - \int_\Omega \boldsymbol{b} \cdot \boldsymbol{u}\mathrm{d}\Omega - \int_{\partial\Omega_t} \bar{\boldsymbol{t}} \cdot \boldsymbol{u}\mathrm{d}\partial\Omega_t \tag{15}$$

where u and p are displacement tensor and fluid pressure. ψ represents elastic strain energy, and ε is the strain tensor. G_c is the critical energy release rate. b is the body force, and $\bar{t}$ is the traction on the boundary $\partial\Omega$t.

Acid dissolution degrades the rock's elastic modulus [30,31], with Young's modulus exhibiting exponential decline with increasing dissolution-induced porosity. It is used to a chemical damage variable [32,33]:

$$d_{\text{chem}} = e^{-r|\Delta\phi|} \tag{16}$$

where r is a degradation coefficient, derived by fitting experimental results [24,34].

Using the phase field method, the total energy functional is as follows [24]:

$$\Psi(\boldsymbol{u}, d, p) = \int_\Omega g(d, d_{\text{chem}}) \psi_+(\boldsymbol{\varepsilon}) + \psi_-(\boldsymbol{\varepsilon}) \mathrm{d}\Omega + \int_\Omega \frac{G_c}{2} \left[l_0 \nabla d \cdot \nabla d + \frac{d^2}{l_0} \right] d\Omega \\ - \int_\Omega \alpha p \cdot (\nabla \cdot \boldsymbol{u}) \mathrm{d}\Omega - \int_\Omega \boldsymbol{b} \cdot \boldsymbol{u} \mathrm{d}\Omega - \int_{\partial\Omega_t} \bar{\boldsymbol{t}} \cdot \boldsymbol{u} \mathrm{d}\partial\Omega_t \tag{17}$$

where g is the degradation function. $\psi+$ and $\psi-$ are tensile and compressive elastic strain energies. d denotes the phase field, and l_0 is a characteristic length parameter.

Integrating crack phase field and chemical damage field influences, the degradation function is as follows:

$$g(d, d_{\text{chem}}) = (1 - k_0)[d_{\text{chem}}(1 - d)]^2 + k_0 \tag{18}$$

where k_0 ensures the stiffness matrix remains well conditioned as the phase field approaches 1.

Using the variational approach, the governing equations for rock deformation are as follows:

$$\nabla \cdot (\boldsymbol{\sigma} - \alpha p \boldsymbol{I}) + \boldsymbol{b} = 0 \tag{19}$$

Similarly, the phase field governing equation, with local history variable $\mathcal{H}$ is as follows:

$$\left[\frac{2l_0(1 - k_0)d_{\text{chem}}^2 \psi_+}{G_c} + 1 \right] d - l_0^2(\nabla d \cdot \nabla d) = \frac{2l_0(1 - k_0)d_{\text{chem}}^2 \mathcal{H}}{G_c} \tag{20}$$

Initial and natural fractures are modeled by prescribing strain field history, as proposed by Borden et al. [35]:

$$\mathcal{H}_0(\boldsymbol{x}) = \begin{cases} \frac{BG_c}{4l_0}\left(1 - \frac{s(\boldsymbol{x},l)}{l_0}\right), & s(\boldsymbol{x}, l) \leq l_0 \\ 0, & s(\boldsymbol{x}, l) > l_0 \end{cases} \tag{21}$$

where B is a constant. $s(\boldsymbol{x},l)$ represents the distance of point x to line l.

3. Numerical Methods

The governing equations are highly nonlinear, necessitating an iterative algorithm for solutions. A hybrid method utilizes the finite element method for stress and phase field discretization and the finite volume method for fluid pressure and acid concentration discretization. The fixed stress split method accelerates convergence due to stress and pressure coupling.

Within the finite element framework, weak formulations of stress and phase field equations are obtained by applying the virtual work principle:

$$\int_\Omega (\boldsymbol{\sigma} - \alpha p \boldsymbol{I}) : \boldsymbol{\varepsilon}(\delta \boldsymbol{u}) \mathrm{d}\Omega = \int_\Omega \boldsymbol{b} \cdot \delta \boldsymbol{u} \mathrm{d}\Omega + \int_{\partial\Omega_t} \bar{\boldsymbol{t}} \cdot \delta \boldsymbol{u} \mathrm{d}\partial\Omega_t \tag{22}$$

$$\int_\Omega \left[2(1 - k_0)d_{\text{chem}}^2 \mathcal{H} + \frac{G_c}{l_0} \right] d\delta d \mathrm{d}\Omega + \int_\Omega G_c l_0 \nabla d \cdot \nabla(\delta d) \mathrm{d}\Omega = 2 \int_\Omega (1 - k_0) d_{\text{chem}}^2 \mathcal{H} \delta d \mathrm{d}\Omega \tag{23}$$

where δu denotes the virtual displacement tensor, and δd represents the virtual phase field variable.

Within the finite volume framework, the fluid pressure integration equation over elements yields the following:

$$\int_{\Omega_e} S_t \frac{\partial p}{\partial t} dV - \int_{\Omega_e} \nabla \cdot \left(\frac{k_t}{\mu} \nabla p \right) dV = \int_{\Omega_e} Q_0 - \frac{R(C_s)a_v\alpha_d}{\rho_s} dV - \int_{\Omega_e} \alpha_t \frac{\partial \varepsilon_{vol}}{\partial t} dV \qquad (24)$$

The flow flux between elements relies on the flow conductivity at the interaction boundary, calculated by the harmonic mean.

Similarly, the acid concentration integration equation is as follows:

$$\int_{\Omega_e} \frac{\partial(\phi C_f)}{\partial t} dV + \int_{\Omega_e} \nabla \cdot (v C_f) dV = \int_{\Omega_e} \nabla \cdot (\phi D_e \cdot \nabla C_f) dV - \int_{\Omega_e} \frac{k_c k_s a_v}{k_c + k_s} C_f dV \qquad (25)$$

Using the upwind scheme for advection flux and harmonic mean for diffusion flux, time derivation is generally estimated by the backward scheme.

Discretized field equations are solved using an efficient iterative algorithm. At each new time step, fluid pressure, displacement, and phase field are iterated using staggered manner until convergence, and then acid concentration is solved based on fluid pressure updates in a decoupled manner. Porosity and property parameters are updated for the next time step. Detailed methods can be found in the previous study [24].

4. Simulation Results

The hydro-mechano-reactive flow coupled model for simulating acid fracture propagation has been validated in a previous study [24], including the calculations of acid dissolution and crack propagation. To further verify its applicability to fracture interaction problems, we examined the scenario of a hydraulic fracture approaching a natural fracture, as this configuration has been extensively studied both experimentally and theoretically. Subsequently, we employed the model to investigate the interaction modes between acid fractures and natural fractures, followed by a comparative analysis of the propagation patterns of acid fractures and hydraulic fractures. Finally, we conducted a comprehensive analysis of the combined effects of acid dissolution and other factors (including stress differential, approach angle, injection rate, and acid concentration) on fracture propagation.

4.1. Verification of Interaction Between Hydraulic Fracture and Natural Fracture

The interaction between hydraulic fractures and pre-existing natural fractures has been a subject of significant research in the field of hydraulic fracturing. Blanton's seminal work [36], which involved experimental studies, led to the development of an interaction criterion that examines the effects of approaching angle and stress difference on fracture behavior. To validate our numerical model against Blanton's established criterion, we simplified our hydro-mechano-reactive flow coupled model to simulate hydraulic fracture propagation by omitting acid transport processes. This allows for a direct comparison between our numerical solutions and Blanton's experimental criterion, thereby providing a robust verification of our model's capability to accurately simulate fracture interactions in the absence of chemical reactions.

Our simulation setup comprises a square sample containing an initial hydraulic fracture and an inclined natural fracture, similar to the configuration illustrated in Figure 2. The domain is discretized into a uniform grid of square elements, with 100 elements along each axis, resulting in a 100×100 mesh. The key distinction in this verification study is the absence of acid in the fracturing fluid. By systematically varying the approaching angle and stress difference in our simulations, we aim to reproduce the interaction behaviors observed in Blanton's experiments. Table 1 presents the model parameters used in these simulations.

Numerical solutions reveal two primary modes when a hydraulic fracture approaches a natural fracture: crossing and diversion. We obtained propagation modes under various scenarios with different approaching angles and stress differences, comparing them with Blanton's criterion as illustrated in Figure 3. In this figure, the region to the right

of Blanton's criterion represents crossing, while the left represents no crossing. Our solution demonstrates consistency with Blanton's criterion, thereby validating the model's application for hydraulic fracture and natural fracture interaction.

Table 1. Input parameters for hydraulic fracture propagation with natural fracture.

Parameter	Symbol	Value	Unit
Length of domain	L	0.5	m
Height of domain	H	0.5	m
Length of initial hydraulic fracture	l_{hf}	0.15	m
Length of natural fracture	l_{nf}	0.1	m
Young's modulus	E	25	GPa
Poisson's ratio	v	0.25	-
Characteristic length parameter	l_0	0.01	-
Critical energy release rate	G_c	50	Pa·m
Maximum principal stress	σ_H	8	MPa
Minimum principal stress	σ_h	5	MPa
Matrix permeability	k_r	1.0×10^{-15}	m^2
Fracture permeability	k_f	1.0×10^{-8}	m^2
Injection rate	v_0	7.5×10^{-4}	m^2/s
Fluid viscosity	μ	1.0×10^{-3}	Pa·s
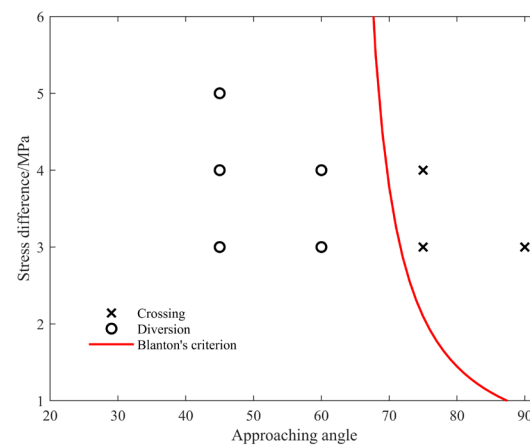
Figure 3. Comparison of fracture propagation mode between our solution and Blanton's criterion.

The phase field method employed in our model automatically determines the hydraulic fracture propagation direction without additional criteria. The fracture always propagates along the path of least energy dissipation. Figure 4 illustrates fracture propagation paths under different approaching angles with a stress difference of 3 MPa.
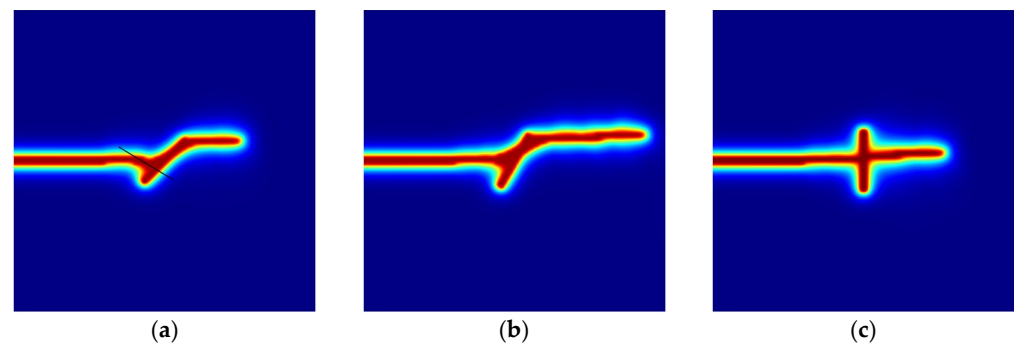
Figure 4. Fracture propagation paths under different approaching angles: (**a**) $\beta = 45°$; (**b**) $\beta = 60°$; (**c**) $\beta = 90°$.

When the approaching angle is 45°, the hydraulic fracture exhibits minimal diversion before contacting the natural fracture (denoted by the black line). It then diverts into the natural fracture, ultimately reinitiating from the tip of the natural fracture and continuing to extend. At a 60° approaching angle, the hydraulic fracture propagates towards the natural fracture and diverts into it. When the approaching angle is 90°, the hydraulic fracture crosses the natural fracture without diversion. These results can be explained by the principle of least energy dissipation. Two main energies are dissipated during fracture propagation: fracture surface energy and elastic strain energy. When a hydraulic fracture approaches a natural fracture at a small angle, it diverts into the natural fracture due to significantly lower fracture surface energy, despite potentially increased dissipated elastic strain energy compared to crossing the natural fracture. However, as the approaching angle increases, the dissipated elastic strain energy along the natural fracture direction increases, making fracture crossing the path of least total energy dissipation.

Figure 5 presents the injection pressures for different approaching angles. The injection pressure for the 45° approaching angle increases first due to hydraulic fracture diversion before contacting the natural fracture. Injection pressures for 60° and 90° approaching angles increase simultaneously. When the hydraulic fracture diverts into the natural fracture, the dissipated energy is less than that of crossing the natural fracture. Consequently, the peak injection pressure is highest when the hydraulic fracture crosses the natural fracture at a 90° approaching angle.
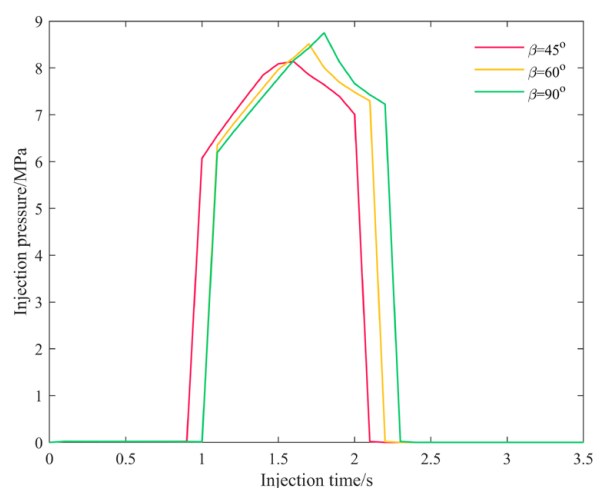
Figure 5. Evolution of injection pressures for different approaching angles.

4.2. Interaction Mode Between Acid Fracture and Natural Fracture

To investigate the interaction mode between acid fractures and natural fractures, we employ a model comprising a square sample with an initial acid fracture and an inclined fracture, as illustrated in Figure 2. It takes approximately 30 min of computation time on an Intel Core i7-6700 CPU.

Our model incorporates reservoir heterogeneity by describing porosity and mineral inclusions using the Weibull distribution. We estimate the macroscopic mechanical parameters using a two-step homogenization method. Table 2 provides the model parameters used in the simulation. Figure 6 presents the distribution of porosity, the volume fraction of mineral inclusions, and the resulting elastic modulus. The heterogeneity in porosity influences acid dissolution and wormhole formation, which, in combination with the heterogeneity in elastic modulus, significantly affects fracture propagation.

Table 2. Input parameters for acid fracture propagation with natural fracture.

Parameter	Symbol	Value	Unit
Length of domain	L	0.5	m
Height of domain	H	0.5	m
Length of initial hydraulic fracture	l_{hf}	0.15	m
Length of natural fracture	l_{nf}	0.1	m
Approaching angle	β	90	$^\circ$
Characteristic length parameter	l_0	0.01	
Critical energy release rate	G_c	50	Pa·m
Elastic modulus of solid matrix	E_m	12	GPa
Poisson's ratio of solid matrix	v_m	0.25	-
Elastic modulus of mineral inclusion	E_i	98	GPa
Poisson's ratio of mineral inclusion	v_i	0.15	-
Scale parameter of f_p		0.12	-
Shape parameter of f_p		10	-
Scale parameter of f_i		0.4	-
Shape parameter of f_i		10	-
Maximum principal stress	σ_H	8	MPa
Minimum principal stress	σ_h	5	MPa
Acid concentration	C_{f0}	0.15	–
Acid injection rate	v_0	1.05×10^{-3}	m^2/s
Acid surface reaction rate	k_s	2.0×10^{-3}	m/s
Molecular diffusion coefficient	D_m	3.6×10^{-9}	m^2/s
Asymptotic Sherwood number	Sh_∞	3.66	–
Constants	$\alpha_{os}, \lambda_X, \lambda_T$	0.5, 0.5, 0.1	–
Initial average permeability	kr	1.0×10^{-15}	m^2
Initial specific surface area	α_0	5.0×10^3	m^{-1}
Initial pore diameter	d_0	1.0×10^{-5}	M
Pore broadening parameter	β	1	–
Chemical degradation coefficient	r	5	-
Fluid viscosity	μ	1.0×10^{-3}	Pa·s
Rock density	ρ_s	2.71×10^3	kg/m^3

(a)   (b)   (c)
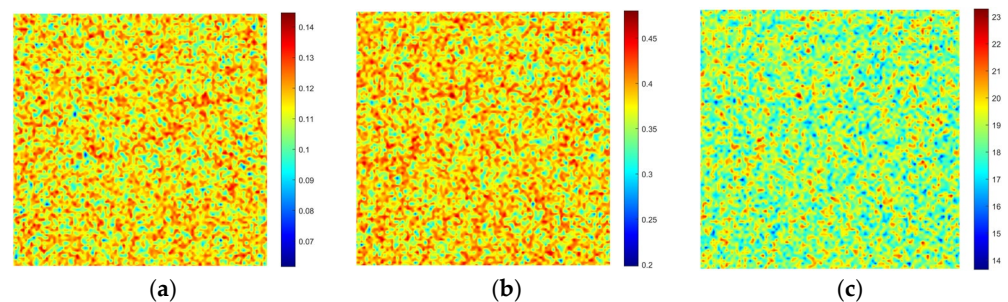
Figure 6. Distribution of reservoir parameters: (**a**) porosity; (**b**) volume fraction of mineral inclusion; (**c**) elastic modulus (GPa).

The acid fracture propagation path, determined using the input data from Table 2, is illustrated in Figure 7a. In this scenario, the acid fracture crosses the natural fracture. To explore additional interaction modes between acid fractures and natural fractures, we adjusted certain parameters. When the stress difference is reduced to 0, the acid fracture diverts into the natural fracture, as shown in Figure 7b. When the injection rate is decreased to 0.75×10^{-3} m^2/s, the acid fracture is arrested by the natural fracture, as depicted in Figure 7c.
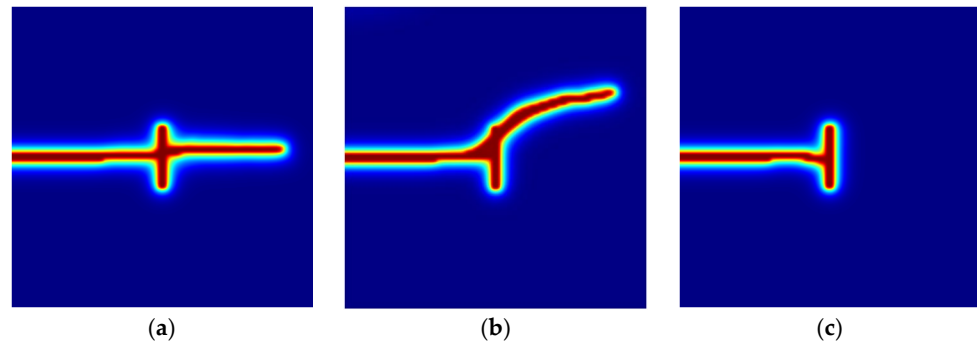
Figure 7. Interaction modes between acid fracture and natural fracture: (**a**) crossing; (**b**) diversion; (**c**) arresting.

Figure 8 presents the porosity distributions under different modes. When the hydraulic fracture contacts the natural fracture, fluid rapidly flows into the natural fracture due to its high permeability. This leads to wormhole formation around both the acid and natural fractures. The distribution of porosity is similar to the previous solution present by Zhu et al. [37]. Comparing Figure 8a,b, we observe that decreasing the stress difference causes the hydraulic fracture to divert into the natural fracture. This phenomenon can be explained by the principle of least energy dissipation. The injection pressures for these two scenarios are similar, as shown in Figure 9. In the arresting mode (Figure 8c), the reduced injection rate results in the formation of numerous wormholes propagating towards the outer boundaries. This causes rapid pressure dissipation, preventing the accumulation of high pressure necessary for the hydraulic fracture to reinitiate from the natural fracture, as evident in Figure 9.
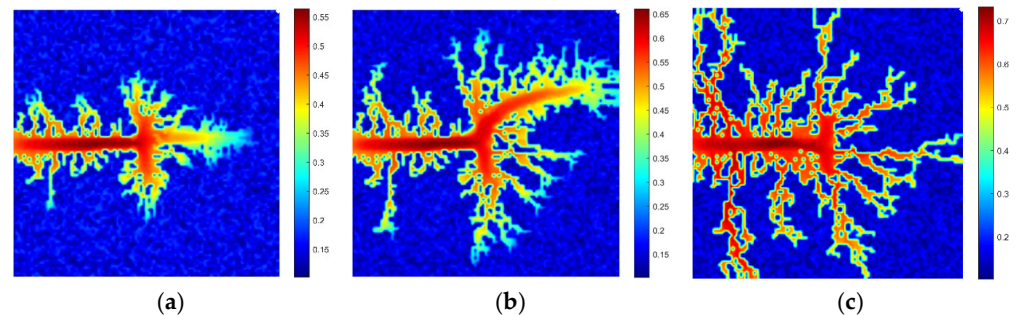
Figure 8. Porosity distributions under different modes: (**a**) crossing; (**b**) diversion; (**c**) arresting.
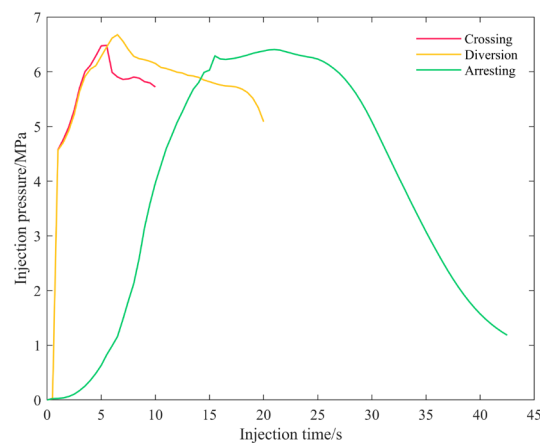
Figure 9. Injection pressure evolution for different modes.

Figure 10 displays the pressure distributions under different modes. The high-pressure area expands as the interaction mode changes from crossing to diversion and then to arresting. In the former modes, especially the crossing mode, pressure dissipation is primarily used to extend fractures. The pressure distribution is also closely related to the wormhole distribution.
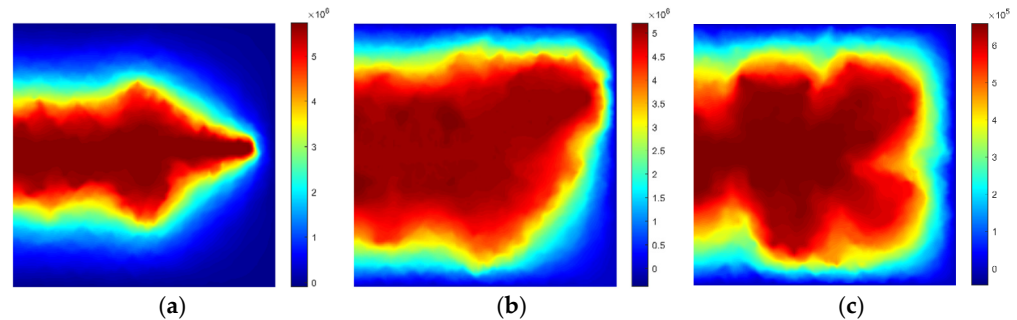
Figure 10. Pressure distributions under different modes: (**a**) crossing; (**b**) diversion; (**c**) arresting.

4.3. Comparison of Propagation Modes: Acid Fracture vs. Hydraulic Fracture

Acid fracturing involves acid transport and dissolution, which significantly influences the interaction process between acid fractures and natural fractures. This leads to distinct propagation modes for acid fractures compared to hydraulic fractures. To investigate the effect of acid dissolution on fracture propagation modes, we conducted several case studies.

Initially, we simulated hydraulic fracture propagations under stress differences of 0 MPa and 3 MPa, with an injection rate of 0.75×10^{-3} m^2/s. Other model parameters remained consistent with those in Table 2. These simulations resulted in diversion and crossing modes, as illustrated in Figures 10b and 11a, respectively.
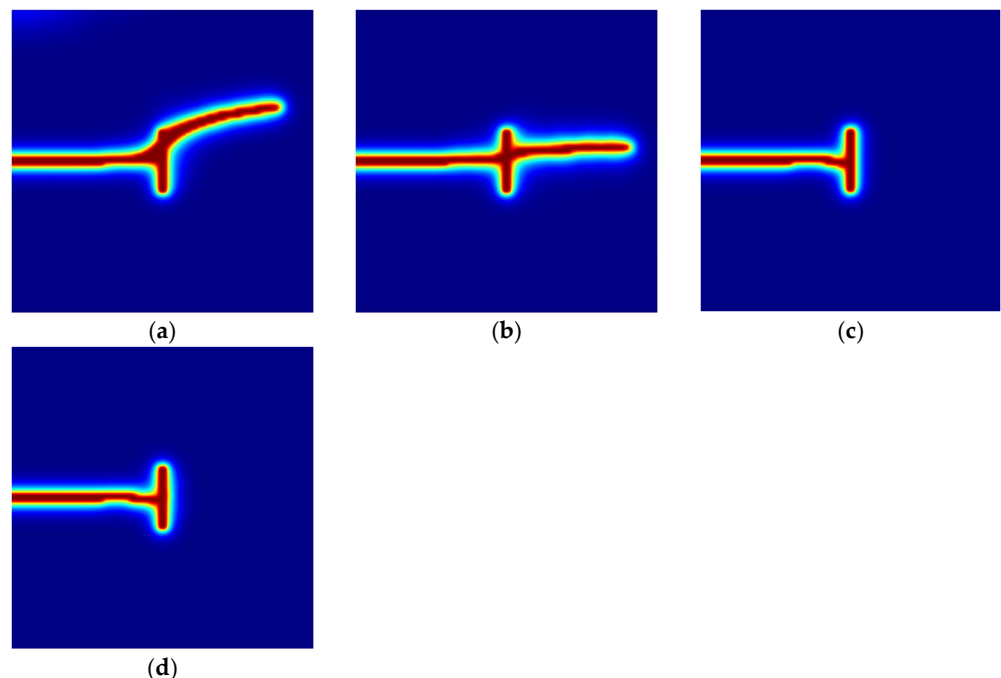
Figure 11. Fracture propagation modes for different cases: (**a**) $\Delta\sigma$ = 0 MPa, hydraulic fracture; (**b**) $\Delta\sigma$ = 3 MPa, hydraulic fracture; (**c**) $\Delta\sigma$ = 0 MPa, acid fracture; (**d**) $\Delta\sigma$ = 3 MPa, acid fracture.

Using the same injection rate, we then calculated acid fracture propagations under the two stress differences. Contrary to hydraulic fractures, acid fractures were arrested by the natural fracture in both cases, as shown in Figures 10d and 11c. The arrest mode of acid fracture is similar to the results presented by Guo et al. [34].

We compared the injection pressure evolutions for these scenarios, as depicted in Figure 12. For hydraulic fracturing, the fluid pressure rises rapidly, enabling the hydraulic fracture to either cross the natural fracture or reinitiate after diversion. In contrast, during acid fracturing, the fluid pressure increases more slowly, and the peak pressure is insufficient for fracture initiation from the natural fracture. This difference is attributed to acid dissolution leading to the formation of numerous wormholes. Fluid flows into these high-permeability channels, preventing the accumulation of high pressure necessary for acid fracture re-initiation.
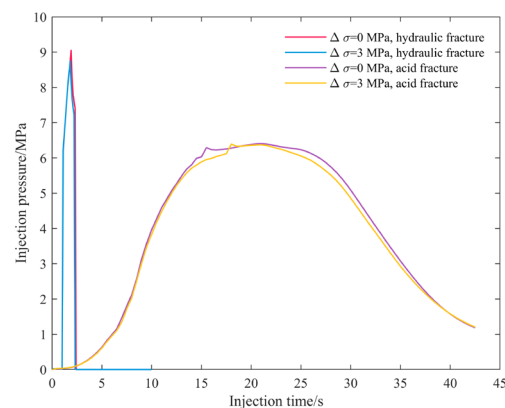
Figure 12. Injection pressure evolution for hydraulic fracture and acid fracture.

These results indicate that the hydraulic fracture is more likely to cross natural fractures, whereas acid fractures tend to become arrested or diverted. This behavior primarily results from wormhole formation due to acid dissolution, which impedes the buildup of high fluid pressure required for fracture initiation and extension.

4.4. Comprehensive Influences of Acid Dissolution with Other Factors

The interaction between acid fractures and natural fractures results from a complex interplay of acid dissolution and other factors, including stress difference, approaching angle, and treatment parameters. To investigate these effects, several scenarios were simulated for acid fracture propagation with natural fractures. Unless otherwise stated, model parameters are as provided in Table 2.

Acid fracture propagations under varying stress differences (0 MPa, 3 MPa, and 5 MPa) are illustrated in Figure 13. At a stress difference of 0 MPa, the acid fracture diverts into the natural fracture and reinitiates from the tip, extending along an arc-shaped path rather than following its initial direction. As the stress difference increases, the fracture propagation mode transitions from diversion to crossing because more strain energy is required for fracture diversion when increasing the principal stress perpendicular to the natural fracture.

| (a) | (b) | (c) |
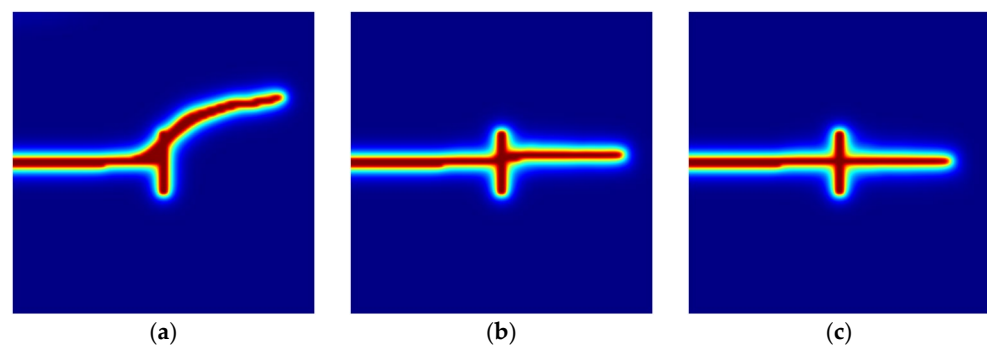
Figure 13. Fracture propagation paths under different stress differences: (**a**) $\Delta\sigma = 0$ MPa; (**b**) $\Delta\sigma = 3$ MPa; (**c**) $\Delta\sigma = 5$ MPa.

Acid fracture approaches to natural fractures at different angles (30°, 60°, and 90°) are illustrated in Figure 14. At angles of 30° and 60°, the acid fracture diverts into the natural fracture. However, with a 30° approach angle, the fracture alters its trajectory before contact and reinitiates at the natural fracture tip. At 60°, the direction remains unchanged until contact and then reinitiates near the tip. At lower approach angles (30° and 60°), the stress concentration at the tip of the natural fracture tends to attract and redirect the approaching acid fracture. This redirection is more pronounced at 30° due to the greater alignment with the natural fracture's orientation. The stress field perturbation becomes significant enough to alter the acid fracture's trajectory even before direct contact. In contrast, at 90°, the acid fracture crosses the natural fracture. This phenomenon is similar to hydraulic fracture propagation. These insights highlight the critical importance of understanding the geometric relationship between induced fractures and the natural fracture network for effective subsurface engineering applications.

(a)　　　　　　　　(b)　　　　　　　　(c)
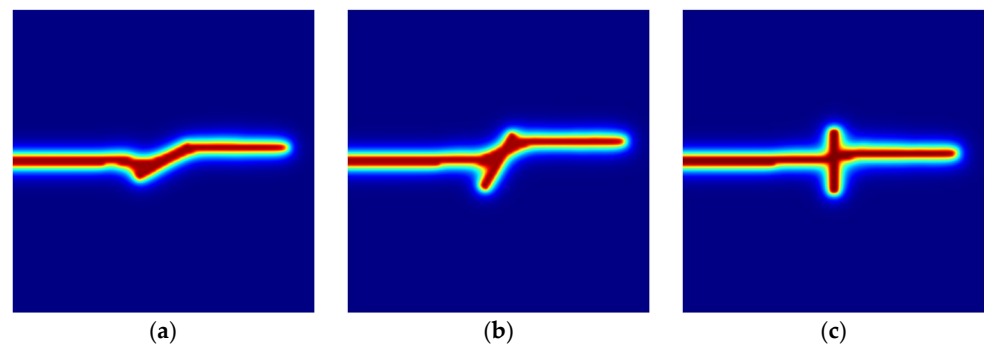
Figure 14. Fracture propagation paths with different approaching angles: (**a**) $\beta = 30°$; (**b**) $\beta = 60°$; (**c**) $\beta = 90°$.

Acid fracture propagation under varying injection rates is presented in Figure 15. At a low injection rate, the acid fracture is arrested by the natural fracture. This behavior can be attributed to insufficient pressure buildup within the fracture. The slower rate allows more time for acid–rock interaction, potentially leading to excessive etching and wormhole formation near the natural fracture interface. This increased permeability can dissipate fluid pressure, preventing the necessary stress concentration for fracture propagation beyond the natural fracture.

(a)　　　　　　　　(b)　　　　　　　　(c)
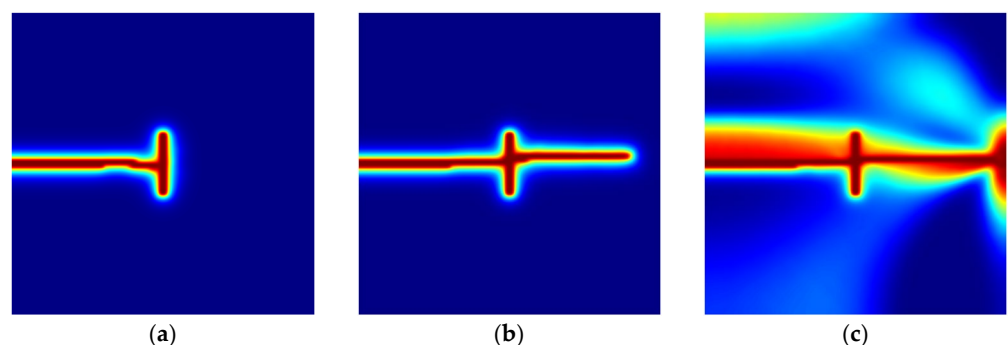
Figure 15. Fracture propagation paths under different injection rates: (**a**) $v_0 = 0.75 \times 10^{-3}$ m^2/s; (**b**) $v_0 = 1.05 \times 10^{-3}$ m^2/s; (**c**) $v_0 = 1.35 \times 10^{-3}$ m^2/s.

Increasing the injection rate leads to the acid fracture crossing the natural fracture. Higher injection rates facilitate high-pressure accumulation in the fracture, promoting fracture re-initiation from the natural fracture. This can be attributed to reduced acid–rock interaction time and enhanced pressure accumulation within the fracture. This scenario closely resembles hydraulic fracturing behavior, where the dominant mechanism shifts from chemical dissolution to mechanical breakdown of the rock formation.

Acid fracture propagations using different acid concentrations are presented in Figure 16. As acid concentration increases, the propagation mode shifts from crossing to arresting or even failure to initiate. While adding acid to the fracturing fluid can reduce breakdown pressure, excessively high concentrations can prevent fracture initiation. This phenomenon is explained by the acid dissolution effect shown in Figure 17.

(a)   (b)   (c)
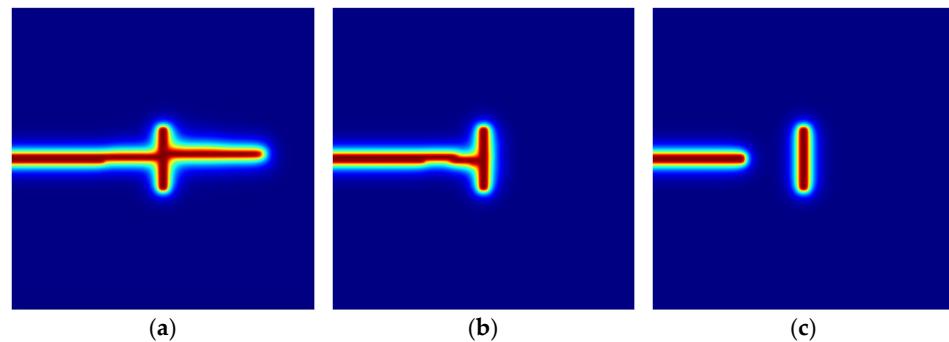
Figure 16. Fracture propagation paths with different acid concentrations: (**a**) C_{f0} = 0.1; (**b**) C_{f0} = 0.15; (**c**) C_{f0} = 0.2.

(a)   (b)   (c)
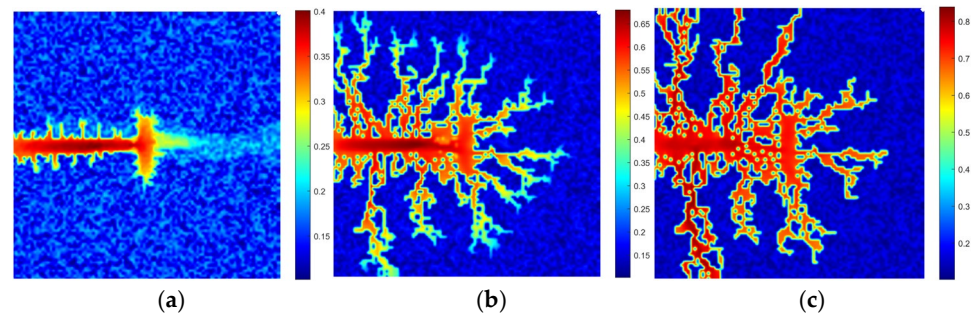
Figure 17. Porosity distributions with different acid concentrations: (**a**) C_{f0} = 0.1; (**b**) C_{f0} = 0.15; (**c**) C_{f0} = 0.2.

The process of acid fracture propagation depends on the dissolution capabilities of the acid used in fracturing fluids. At lower concentrations, the acid efficiently reduces the breakdown pressure by weakening the rock matrix, facilitating fracture initiation and propagation. However, as the concentration increases, the aggressive dissolution forms enhanced permeability channels known as wormholes. These wormholes significantly alter the fluid dynamics within the fracture, allowing hydraulic pressure to dissipate rapidly. Consequently, the pressure necessary for further fracture propagation cannot be sustained, leading to arrest or failure to initiate the fracture. This relationship highlights the dual role of acid as both an enabler and a potential inhibitor of fracture growth, depending on its concentration. To deepen the understanding of this complex interaction, future work could focus on performing experimental validation that varies acid concentration and assessing its effect on fracture propagation.

5. Conclusions

The hydro-mechano-reactive flow coupled model effectively simulates the interaction between acid fractures and natural fractures. It has been validated against established criteria for hydraulic fracturing and successfully extended to acid fracturing scenarios. The following key conclusions are obtained:

(1) Acid fractures exhibit different propagation modes compared to hydraulic fractures when interacting with natural fractures. While hydraulic fractures are more likely to cross natural fractures, acid fractures tend to be arrested due to wormhole formation and pressure dissipation.

(2) Increasing stress differences and approaching angles significantly affect fracture behavior. Higher stress differences promote fracture crossing, while smaller approaching angles favor diversion into natural fractures for both hydraulic and acid fractures.

(3) Injection rate and acid concentration play crucial roles in fracture propagation. Higher injection rates facilitate fracture crossing by increasing pressure accumulation, while excessive acid concentrations can hinder fracture initiation due to enhanced wormhole formation and pressure dissipation.

(4) The model incorporates reservoir heterogeneity, demonstrating that variations in porosity and mineral inclusions significantly influence acid dissolution, wormhole formation, and subsequent fracture propagation patterns. This highlights the importance of considering reservoir heterogeneity in fracture stimulation design.

Data Availability Statement: The data presented in this study are available on request from the corresponding author.

Conflicts of Interest: The authors declare no conflicts of interest.

References

1. Rueda Cordero, J.A.; Mejia Sanchez, E.C.; Roehl, D.; Pereira, L.C. Hydro-Mechanical Modeling of Hydraulic Fracture Propagation and Its Interactions with Frictional Natural Fractures. *Comput. Geotech.* **2019**, *111*, 290–300. [CrossRef]
2. Hu, Y.; Gan, Q.; Hurst, A.; Elsworth, D. Investigation of Coupled Hydro-Mechanical Modelling of Hydraulic Fracture Propagation and Interaction with Natural Fractures. *Int. J. Rock Mech. Min. Sci.* **2023**, *169*, 105418. [CrossRef]
3. Qin, M.; Yang, D.; Jia, Y.; Zhou, Y. Peridynamics Modeling of Hydraulic Fracture Interaction with Natural Fractures in Fractured Rock Mass. *Eng. Fract. Mech.* **2024**, *307*, 110299. [CrossRef]
4. Wang, H.; Yang, S.; Zhou, D.; Wang, Q. Influence of Non-Intersecting Cemented Natural Fractures on Hydraulic Fracture Propagation Behavior. *J. Struct. Geol.* **2024**, *181*, 105111. [CrossRef]
5. Yi, L.-P.; Li, X.-G.; Yang, Z.-Z.; Yang, C.-X. Phase Field Modeling of Hydraulic Fracturing in Porous Media Formation with Natural Fracture. *Eng. Fract. Mech.* **2020**, *236*, 107206. [CrossRef]
6. Zhou, Y.; Yang, D.; Zhang, X.; Chen, W.; Xia, X. Numerical Investigation of the Interaction between Hydraulic Fractures and Natural Fractures in Porous Media Based on an Enriched FEM. *Eng. Fract. Mech.* **2020**, *235*, 107175. [CrossRef]
7. Xiong, D.; Ma, X. Influence of Natural Fractures on Hydraulic Fracture Propagation Behaviour. *Eng. Fract. Mech.* **2022**, *276*, 108932. [CrossRef]
8. Sun, T.; Zeng, Q.; Xing, H. A Quantitative Model to Predict Hydraulic Fracture Propagating across Cemented Natural Fracture. *J. Pet. Sci. Eng.* **2022**, *208*, 109595. [CrossRef]
9. Dehghan, A.N. An Experimental Investigation into the Influence of Pre-Existing Natural Fracture on the Behavior and Length of Propagating Hydraulic Fracture. *Eng. Fract. Mech.* **2020**, *240*, 107330. [CrossRef]
10. Wang, W.; Olson, J.E.; Prodanović, M.; Schultz, R.A. Interaction between Cemented Natural Fractures and Hydraulic Fractures Assessed by Experiments and Numerical Simulations. *J. Pet. Sci. Eng.* **2018**, *167*, 506–516. [CrossRef]
11. Abe, A.; Kim, T.W.; Horne, R.N. Laboratory Hydraulic Stimulation Experiments to Investigate the Interaction between Newly Formed and Preexisting Fractures. *Int. J. Rock Mech. Min. Sci.* **2021**, *141*, 104665. [CrossRef]
12. Zhou, J.; Chen, M.; Jin, Y.; Zhang, G. Analysis of Fracture Propagation Behavior and Fracture Geometry Using a Tri-Axial Fracturing System in Naturally Fractured Reservoirs. *Int. J. Rock Mech. Min. Sci.* **2008**, *45*, 1143–1152. [CrossRef]
13. Zhang, J.; Li, Y.; Pan, Y.; Wang, X.; Yan, M.; Shi, X.; Zhou, X.; Li, H. Experiments and Analysis on the Influence of Multiple Closed Cemented Natural Fractures on Hydraulic Fracture Propagation in a Tight Sandstone Reservoir. *Eng. Geol.* **2021**, *281*, 105981. [CrossRef]
14. Qiu, G.; Chang, X.; Li, J.; Guo, Y.; Zhou, Z.; Wang, L.; Wan, Y.; Wang, X. Study on the Interaction between Hydraulic Fracture and Natural Fracture under High Stress. *Theor. Appl. Fract. Mech.* **2024**, *130*, 104259. [CrossRef]
15. Wang, X.; Chen, J.; Ren, D.; Zhu, J. Role of Natural Fractures with Topology Structure for Hydraulic Fracture Propagation in Continental Shale Reservoir. *Eng. Fract. Mech.* **2023**, *284*, 109237. [CrossRef]
16. Li, Y.; Hu, W.; Wei, S.; Zhang, Z.; Yang, P.; Song, S. Sensitivity Analysis on the Effect of Natural Fractures and Injected Fluid on Hydraulic Fracture Propagation in a Fractured Reservoir. *Eng. Fract. Mech.* **2022**, *263*, 108288. [CrossRef]

17. Tong, L.; Xiaochen, W.; Xiangjun, L.; Lixi, L.; Xuancheng, W.; Jin, C.; Hongwei, L. A Criterion for a Hydraulic Fracture Crossing a Natural Fracture in Toughness Dominant Regime and Viscosity Dominant Regime. *Eng. Fract. Mech.* **2023**, *289*, 109421. [CrossRef]
18. Dang, L.; Zhou, C.; Huang, M.; Jiang, D. Simulation of Effective Fracture Length of Prepad Acid Fracturing Considering Multiple Leak-off Effect. *Nat. Gas Ind. B* **2019**, *6*, 64–70. [CrossRef]
19. Dong, R.; Wheeler, M.F.; Ma, K.; Su, H. A 3D Acid Transport Model for Acid Fracturing Treatments with Viscous Fingering. In Proceedings of the SPE Annual Technical Conference and Exhibition, Virtual, 26–29 October 2020.
20. Ugursal, A.; Zhu, D.; Hill, A.D. Development of Acid Fracturing Model for Naturally Fractured Reservoirs. *SPE Prod. Oper.* **2019**, *34*, 735–748. [CrossRef]
21. Dai, Y.; Hou, B.; Zhou, C.; Zhang, K.; Liu, F. Interaction Law between Natural Fractures-Vugs and Acid-Etched Fracture during Steering Acid Fracturing in Carbonate Reservoirs. *Geofluids* **2021**, *2021*, 1–16. [CrossRef]
22. Chen, Y.; Ma, G.; Li, T.; Wang, Y.; Ren, F. Simulation of Wormhole Propagation in Fractured Carbonate Rocks with Unified Pipe-Network Method. *Comput. Geotech.* **2018**, *98*, 58–68. [CrossRef]
23. Zhu, T.; Wei, X.; Zhang, Z. Numerical Simulation of Hydraulic-Mechanical-Chemical Field Coupled Acid Fracturing in Complex Carbonate Reservoir. *Comput. Geotech.* **2023**, *156*, 105277. [CrossRef]
24. Zeng, Q.; Li, T.; Liu, P.; Bo, L.; Yao, C.; Yao, J. A Phase Field Framework to Model Acid Fracture Propagation with Hydro-Mechano-Reactive Flow Coupling. *Comput. Geotech.* **2024**, *174*, 106658. [CrossRef]
25. Zhao, J.J.; Shen, W.Q.; Shao, J.F.; Liu, Z.B.; Vu, M.N. A Constitutive Model for Anisotropic Clay-Rich Rocks Considering Micro-Structural Composition. *Int. J. Rock Mech. Min. Sci.* **2022**, *151*, 105029. [CrossRef]
26. Yu, Z.; Shao, J.; Sun, Y.; Wang, M.; Vu, M.; Plua, C. Numerical Analysis of Hydro-Thermal Fracturing in Saturated Rocks by Considering Material Anisotropy and Micro-Structural Heterogeneity. *Int. J. Rock Mech. Min. Sci.* **2023**, *170*, 105457. [CrossRef]
27. Giraud, A.; Huynh, Q.V.; Hoxha, D.; Kondo, D. Application of Results on Eshelby Tensor to the Determination of Effective Poroelastic Properties of Anisotropic Rocks-like Composites. *Int. J. Solids Struct.* **2007**, *44*, 3756–3772. [CrossRef]
28. Lee, S.; Wheeler, M.F.; Wick, T. Pressure and Fluid-Driven Fracture Propagation in Porous Media Using an Adaptive Finite Element Phase Field Model. *Comput. Methods Appl. Mech. Eng.* **2016**, *305*, 111–132. [CrossRef]
29. Panga, M.K.R.; Ziauddin, M.; Balakotaiah, V. Two-Scale Continuum Model for Simulation of Wormholes in Carbonate Acidization. *AIChE J.* **2005**, *51*, 3231–3248. [CrossRef]
30. Palchik, V.; Hatzor, Y.H. Crack Damage Stress as a Composite Function of Porosity and Elastic Matrix Stiffness in Dolomites and Limestones. *Eng. Geol.* **2002**, *63*, 233–245. [CrossRef]
31. Croizé, D.; Bjørlykke, K.; Jahren, J.; Renard, F. Experimental Mechanical and Chemical Compaction of Carbonate Sand. *J. Geophys. Res.* **2010**, *115*, B11204. [CrossRef]
32. Wojtacki, K.; Lewandowska, J.; Gouze, P.; Lipkowski, A. Numerical Computations of Rock Dissolution and Geomechanical Effects for CO_2 Geological Storage. *Int. J. Numer. Anal. Methods Geomech.* **2015**, *39*, 482–506. [CrossRef]
33. Schuler, L.; Ilgen, A.G.; Newell, P. Chemo-Mechanical Phase-Field Modeling of Dissolution-Assisted Fracture. *Comput. Methods Appl. Mech. Eng.* **2020**, *362*, 112838. [CrossRef]
34. Guo, Y.; Na, S. A Reactive-Transport Phase-Field Modelling Approach of Chemo-Assisted Cracking in Saturated Sandstone. *Comput. Methods Appl. Mech. Eng.* **2024**, *419*, 116645. [CrossRef]
35. Borden, M.J.; Verhoosel, C.V.; Scott, M.A.; Hughes, T.J.R.; Landis, C.M. A Phase-Field Description of Dynamic Brittle Fracture. *Comput. Methods Appl. Mech. Eng.* **2012**, *217–220*, 77–95. [CrossRef]
36. Blanton, T.L. An Experimental Study of Interaction between Hydraulically Induced and Pre-Existing Fractures. In Proceedings of the SPE Unconventional Gas Recovery Symposium, Pittsburgh, PA, USA, 16–18 May 1982; pp. 559–571.
37. Zhu, T.; Zhang, Z.; Liu, Z.; An, N.; Wei, X. Simulation of hydraulic-mechanical-chemical coupled acid fracturing of rock with lattice bonds. *Heliyon* **2024**, *10*, e26517. [CrossRef]